



Cite this: DOI: 10.1039/d2cp01961b

An accurate $\text{NH}_2(\text{X}^2\text{A}'')$ CHIPR potential energy surface *via* extrapolation to the complete basis set limit and dynamics of the $\text{N}(\text{D}) + \text{H}_2(\text{X}^1\Sigma_g^+)$ reaction†

Ximing Li, ^a Zhi Qin, ^{ab} Jing Li^{*c} and Linhua Liu ^{*abd}

The amidogen radical (NH_2) and its associated $\text{N}(\text{D}) + \text{H}_2(\text{X}^1\Sigma_g^+) \rightarrow \text{H}(\text{S}) + \text{NH}(\text{X}^3\Sigma^-)$ reaction have great significance in interstellar chemistry and the accurate potential energy surface (PES) is the basis for studying them. We report a new and accurate PES for the ground state $\text{NH}_2(\text{X}^2\text{A}'')$ using the combined-hyperbolic-inverse-power-representation methodology based on 7970 *ab initio* energy points computed at the Davidson-corrected internally contracted multireference configuration interaction level of theory. Both aug-cc-pVTZ and aug-cc-pVQZ basis sets have been employed to extrapolate the energies to the complete basis set limit. The analytical PES reproduces well with the *ab initio* energy points with a root mean square deviation of 55.7 cm^{-1} . The topographical features of the analytical PES are examined in detail and agree well with the previous theoretical results. The integral cross sections and rate constants of the $\text{N}(\text{D}) + \text{H}_2(\text{X}^1\Sigma_g^+) \rightarrow \text{H}(\text{S}) + \text{NH}(\text{X}^3\Sigma^-)$ reaction are obtained using the quasi-classical trajectory method and the time-dependent wave packet method and then compared with the available theoretical and experimental values.

Received 29th April 2022,
Accepted 11th October 2022

DOI: 10.1039/d2cp01961b

rsc.li/pccp

1 Introduction

As one of the essential triatomic molecules, the amidogen radical (NH_2) plays an important role in atmospheric and interstellar chemistry.^{1–7} van Dishoeck *et al.*⁸ reported the first absorption of NH_2 in Sgr B2. As it is directly related to ammonia (NH_3), the nitrogen chemical reaction of $\text{N} + \text{H}_2 \rightarrow \text{NH} + \text{H}$ is known as the first step to yield NH_3 in dense interstellar clouds.^{9,10} Because of the low reactivity of the ground state $\text{N}(\text{S})$, the first excited $\text{N}(\text{D})$ and its associated $\text{N}(\text{D}) + \text{H}_2$ insertion reaction, which mainly occurs *via* the ground $\text{X}^2\text{A}''$ potential energy surface (PES), have been the subject of many theoretical and experimental works.

Experimentally, there are several investigations for the dynamics of the $\text{N}(\text{D}) + \text{H}_2/\text{D}_2$ reaction. Dodd *et al.*¹¹ measured the inverted nascent vibrational distributions of $\text{NH}(\text{X}^3\Sigma^-)$ produced by the $\text{N}(\text{D}) + \text{H}_2$ reaction, and the results suggested the direct abstraction type mechanism of the H atom during the reaction. Later, Umemoto *et al.*^{12,13} measured the nascent NH/D vibrational distributions at lower temperatures against those obtained by Dodd *et al.*¹¹ In addition, the rate constants for the $\text{N}(\text{D}) + \text{H}_2/\text{D}_2$ reaction have been measured by several previous works.^{14–22} The first temperature-dependent rate constants for the $\text{N}(\text{D}) + \text{H}_2/\text{D}_2$ reaction over the temperature range of 213–300 K were measured by Suzuki *et al.*¹⁴ Umemoto *et al.*¹⁶ measured the rate constant at 300 K for the $\text{N}(\text{D}) + \text{H}_2/\text{D}_2$ reaction, which agreed well with the results of Suzuki *et al.*¹⁴ Dianailys *et al.*¹⁵ also measured the rate constants for the $\text{N}(\text{D}) + \text{H}_2/\text{D}_2$ reaction from 127 to 296 K, which showed a similar trend to the results of Suzuki *et al.*¹⁴

Theoretically, a London–Eyring–Polanyi–Sato (LEPS) PES was constructed by Suzuki *et al.*¹⁴ to study the Arrhenius parameters for the $\text{N}(\text{D}) + \text{H}_2/\text{D}_2$ reaction using the quasi-classical trajectory (QCT) method. Later, Pederson *et al.*²³ reported a global PES for the ground state $\text{NH}_2(\text{X}^2\text{A}'')$ by fitting to the multireference configuration interaction (MRCI) energy points. During the fitting, a reproducing kernel Hilbert space (RKHS) interpolation method was used to fit 1512 *ab initio* energy points, and the total root mean square deviation (rmsd)

^a School of Energy and Power Engineering, Shandong University, 250061, Jinan, China. E-mail: liulinhua@sdu.edu.cn

^b Optics and Thermal Radiation Research Center, Institute of Frontier and Interdisciplinary Science, Shandong University, 266237, Qingdao, China

^c School of Physics and Physical Engineering, Qufu Normal University, 273165, Qufu, China. E-mail: jing-li@163.com

^d School of Energy Science and Engineering, Harbin Institute of Technology, 150001, Harbin, China

† Electronic supplementary information (ESI) available: The validations of PES, the fitted parameters of the switch function, the parameters used in the time-dependent wave packet calculations, the interpretation of the switch function, and the Fortran code for the CHIPR PES. See DOI: <https://doi.org/10.1039/d2cp01961b>

was about 104.9 cm^{-1} . In addition, the results of the QCT calculations for the $\text{N}(\text{D}) + \text{H}_2/\text{D}_2$ reaction successfully reproduced the product state distributions obtained in experiments.^{12,13} Ho *et al.*²⁴ presented an improved RKHS PES of $\text{NH}_2(\text{X}^2\text{A}')$ based on 2715 high-quality MRCI energy points, which was smoother and enhanced the capability of performing the QCT calculations. The cubic spline method was employed by Qu *et al.*²⁵ to interpolate *ab initio* energy points of the $\text{X}^2\text{A}''$ and $\text{A}^2\text{A}'$ states of NH_2 from the MRCI/aug-cc-pVQZ (AVQZ) calculation. The subsequent room-temperature rate constants obtained from the QCT calculations were in good agreement with those measured by their experiments. Varandas and Poveda²⁶ reported the first single-sheeted double many-body expansion (DMBE) PES of $\text{NH}_2(\text{X}^2\text{A}')$ by fitting 1498 MRCI/AVQZ *ab initio* energy points, and the total rmsd was 165.8 cm^{-1} . They also employed a novel switching function to guarantee the $\text{N} + \text{H}(\text{S}) + \text{H}(\text{S})$ dissociation asymptote at the $\text{N}(\text{D}) + \text{H}_2(\text{X}^1\Sigma_g^+)$ and $\text{H}(\text{S}) + \text{NH}(\text{X}^3\Sigma^-)$ dissociation channels. Based on the above-mentioned DMBE PES²⁶ of $\text{NH}_2(\text{X}^2\text{A}')$, Chu *et al.*²⁷ reported a dynamic study of the $\text{N}(\text{D}) + \text{H}_2$ ($\nu = 0, j = 1-5$) $\rightarrow \text{H}(\text{S}) + \text{NH}(\text{X}^3\Sigma^-)$ reaction using the time-dependent quantum wave packet method. In addition, Li *et al.*⁷ reported a more accurate DMBE PES of $\text{NH}_2(\text{X}^2\text{A}')$ based on 2102 *ab initio* energy points, which were calculated at the multireference configuration interaction level including Davidson corrections [MRCI(Q)] using the aug-cc-pVTZ (AVTZ) and AVQZ basis sets. The MRCI(Q)/AV(T,Q)Z energies were extrapolated to the complete basis set (CBS) limit, and the total rmsd was 243.1 cm^{-1} . Subsequently, the reaction probabilities, integral cross sections (ICSSs) and differential cross sections (DCSSs) of the $\text{N}(\text{D}) + \text{H}_2$ ($\nu = 0, j = 0$) $\rightarrow \text{H}(\text{S}) + \text{NH}(\text{X}^3\Sigma^-)$ reaction were calculated using the quantum wave packet method. Moreover, based on the PES of Li *et al.*,⁷ Zheng and Zhu⁴ carried out the dynamic calculations of the $\text{N}(\text{D}) + \text{H}_2/\text{HD}/\text{D}_2$ reactions using the time dependent wave packet method. The reaction probabilities, DCSSs and ICSSs were obtained and compared with the previous theoretical and experimental values. Dianailys *et al.*¹⁵ reported an experimental and theoretical study of the $\text{N}(\text{D}) + \text{H}_2/\text{D}_2$ reaction, and the rate constants obtained from the experiments and calculations were in good agreement at room temperature. Based on the PES modeled by Li and Varandas,²⁸ Peng *et al.*²⁹ performed a quantum wave packet calculation for the $\text{N}(\text{D}) + \text{H}_2(\text{X}^1\Sigma_g^+)$ reaction and obtained the reaction probabilities and ICSSs at various total angular momentum J .

The rate constants^{14-22,76} for the $\text{N}(\text{D}) + \text{H}_2$ reaction were mainly measured at room temperature (300 K), excluding the works of Suzuki *et al.*¹⁴ and Dianailys *et al.*¹⁵ In 1993, Suzuki *et al.*¹⁴ first measured the temperature-dependent rate constants over the 213–300 K temperature range. Recently, Dianailys *et al.*¹⁵ extended the values to 127–296 K. Most theoretical studies^{68,71} showed good agreement with the experimental rate constants^{14,15} over the 213–300 K temperature range but underestimated the measured values¹⁵ for temperatures below 200 K. Since the treatment of the reaction dynamic calculation for the title system is mature, the bottleneck for a quantitative characterization of the reaction dynamics becomes the PES.

In addition, most dynamic studies of the $\text{N}(\text{D}) + \text{H}_2(\text{X}^1\Sigma_g^+)$ reaction focused on the effects of reactant rotational quantum numbers j on the reactivity, ignoring the influences of the reactant vibrational excitation on the reactivity. Thus, the purpose of this work is dual. First, we report a new PES of the ground state $\text{NH}_2(\text{X}^2\text{A}')$. The PES is modeled using the combined-hyperbolic-inverse-power-representation (CHIPR) method^{30,31} with the high-quality MRCI(Q) energy points. The rmsd of the novel PES from the *ab initio* results is only 55.7 cm^{-1} . Second, for a deeper understanding of the $\text{N}(\text{D}) + \text{H}_2(\text{X}^1\Sigma_g^+) \rightarrow \text{H}(\text{S}) + \text{NH}(\text{X}^3\Sigma^-)$ reaction, the QCT and the time-dependent wave packet (TDWP) method have been employed to calculate the rate constants below the room temperature and the vibration-dependent ICSSs for the $\text{N}(\text{D}) + \text{H}_2$ reaction.

This article is organized as follows. Section 2 introduces details of the *ab initio* calculations for $\text{NH}_2(\text{X}^2\text{A}')$ and the CBS extrapolation scheme. Section 3 describes the CHIPR fitting method. The topographical characteristics of the CHIPR PES are discussed in Section 4. The QCT and the quantum mechanical (QM) dynamic calculations are carried out in Section 5. Finally, conclusions are drawn in Section 6.

2 *Ab initio* calculations and CBS extrapolation scheme

In this work, the MOLPRO 2015 package^{32,33} was employed to calculate the *ab initio* potential energy points of the ground state $\text{NH}_2(\text{X}^2\text{A}')$. First, the single-configuration wavefunction of $\text{NH}_2(\text{X}^2\text{A}')$ was generated using the Hartree–Fock (HF) method and then it was optimized by the equal weight SA-CASSCF³⁴ calculation for the first two $^2\text{A}''$ states of the NH_2 system to obtain multiconfiguration wavefunctions. Using SA-CASSCF multiconfiguration wave functions as a reference, the subsequent MRCI³⁵ calculations considered the Davidson correction (+Q) to counteract the higher order correlation effect. In all *ab initio* calculations, both AVTZ and AVQZ basis sets³⁶ were employed for the N and H atoms, respectively. Ten active orbitals ($8a' + 2a''$) and one core orbital ($1a'$) were used for seven correlated electrons of the NH_2 radical. The Jacobi coordinates (R, r and θ) were employed to map the PES with 7970 *ab initio* energy points. For the $\text{N} + \text{H}_2$ channel, the ranges were set as $1.2 \leq r_{\text{H-H}}/a_0 \leq 4.0$, $1.6 \leq R_{\text{N-HH}}/a_0 \leq 10.0$ and $0 \leq \theta/\text{deg} \leq 180.0$, and for the $\text{H} + \text{NH}$ geometry, the grids were defined by $1.6 \leq r_{\text{N-H}}/a_0 \leq 4.0$, $1.6 \leq R_{\text{H-NH}}/a_0 \leq 10.0$ and $0 \leq \theta/\text{deg} \leq 180$. In addition, the *ab initio* potential energy points of $\text{H}_2(\text{X}^1\Sigma_g^+)$ and $\text{NH}(\text{X}^3\Sigma^-)$ were calculated at MRCI(Q)/AVXZ ($X = \text{T, Q}$) energy points, which was at the same level of $\text{NH}_2(\text{X}^2\text{A}')$.

To reduce the error of truncation of the one-particle basis set expansion,³⁷ the obtained *ab initio* energies were extrapolated to the CBS limit. For each pair of *ab initio* grid energies calculated using the AVXZ ($X = \text{T, Q}$) basis sets, the approximate CBS limit can be defined as

$$E_X(R) = E_X^{\text{CAS}}(R) + E_X^{\text{dc}}(R) \quad (1)$$

where CAS and dc indicate the complete active space energies and dynamical correlation energies, respectively. Then, the CBS extrapolations were conducted separately for the CAS and dc energies by^{38,39}

$$E_X^{\text{CAS}} = E_{\infty}^{\text{CAS}} + B/X^{\alpha} \quad (2)$$

and

$$E_X^{\text{dc}} = E_{\infty}^{\text{dc}} + \frac{A_3}{(X + \beta)^3} + \frac{A_5}{(X + \beta)^5} \quad (3)$$

where $A_5 = A_5(0) + dA_3^{5/4}$, $\alpha = 5.34$, $\beta = -3/8$, $d = -1.17847713 E_h^{-5/4}$, and $A_5(0) = 0.0037685459$. A_3 and E_{∞}^{dc} are determined by the fitting of the dc energies.

3 CHIPR PES of $\text{NH}_2(\text{X}^2\text{A}'')$

According to the CHIPR method of Varandas,^{30,31} the potential of a triatomic molecule assumes the form of the many-body expansion (MBE)⁴⁰

$$V_{\text{tot}}(R_1, R_2, R_3) = \sum_{i=1}^3 V^{(1)} + \sum_{i=1}^3 V_i^{(2)}(R_i) + V^{(3)}(R_1, R_2, R_3) \quad (4)$$

where V_{tot} is the calculated MRCI(Q)/CBS energy for any geometry of the triatomic molecule, $V^{(1)}$ is the one-body fragment energy, $V_i^{(2)}$ ($i = 1$ for H_2 , 2 and 3 for NH , respectively) and $V^{(3)}$ are the two- and three-body energies, respectively.

For an n -atom molecule, the CHIPR n -body term has the general form^{30,31}

$$V^{(n)} = \sum_{\substack{i_1=0, \\ \dots, \\ i_{\tau}=0}}^L C_{i_1, \dots, i_{\tau}} \prod_{p=1}^{\tau} y_p^{i_p} \quad (5)$$

where $C_{i_1, \dots, i_{\tau}}$ are the expansion coefficients of a L th-order polynomial, y_p is the set of $p = 1, 2, \dots, \tau$ (τ is the number of independent degree of freedom for a n -atom system) coordinates relative to the reference geometry and can be expanded based on a distributed-origin contracted basis set

$$y_p = \sum_{\alpha=1}^M c_{\alpha} \phi_{p,\alpha} \quad (6)$$

where c_{α} is the contraction coefficient and α represents the index of each primitive function $\phi_{p,\alpha}$. The primitive functions assume the following two forms to ensure the correct behavior at both short-range and long-range regions.

(1) If ignoring long-range terms, the function $\phi_{p,\alpha}$ can be chosen as^{30,31}

$$\phi_{p,\alpha} = \text{sech}^{\eta_{\alpha}}(\gamma_{p,\alpha} \rho_{p,\alpha}) \quad (7)$$

(2) If taking long-range terms into account, the following form^{30,31} is a better choice

$$\phi_{p,\alpha} = \left[\frac{\tanh(\beta_{\alpha} R_p)}{R_p} \right]^{\sigma_{\alpha}} \text{sech}^{\eta_{\alpha}}(\gamma_{p,\alpha} \rho_{p,\alpha}) \quad (8)$$

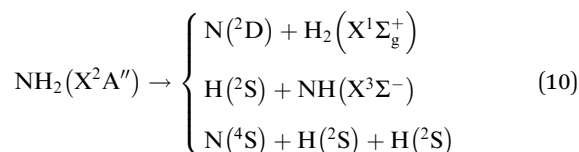
where $\rho_{p,\alpha} = R_p - R_{p,\alpha}^{\text{ref}}$ means the difference between R_p and the primitive's origin $R_{p,\alpha}^{\text{ref}}$. $\gamma_{p,\alpha}$ are non-linear parameters with $\eta_{\alpha} = \eta = 1$, $\sigma_{\alpha} = \sigma = 6$ and $\beta_{\alpha} = \beta = 1/5$. Here, both primitives in eqn (7) and (8) are utilized in the basis set contraction in eqn (6) and eqn (8), which only appears once in the expansion of eqn (6). To reduce linear dependencies, $R_{p,\alpha}^{\text{ref}}$ is obtained by the following relationship

$$R_{p,\alpha}^{\text{ref}} = \zeta(R_p^{\text{ref}})^{\alpha-1} \quad (9)$$

where ζ and R_p^{ref} should be carefully selected during the fitting. To determine the contracted basis sets, the 1D *ab initio* cuts along the NH and HH degrees of freedom have been selected. And relevant calculations are carried out at the global minimum on the PES.

3.1 One-body terms and the switch function

$\text{NH}_2(\text{X}^2\text{A}'')$ follows the dissociation scheme below



The excited $\text{N}(^2\text{D})$ atom only exists at the $\text{N}(^2\text{D}) + \text{H}_2(\text{X}^1\Sigma_g^+)$ dissociation channel, but $\text{NH}(\text{X}^3\Sigma^-)$ dissociates to the ground state $\text{N}(^4\text{S})$. Hence, it is necessary to introduce a function to switch the excited state $\text{N}(^2\text{D})$ to the ground state $\text{N}(^4\text{S})$ in the $\text{N}(^2\text{D}) + \text{H}_2(\text{X}^1\Sigma_g^+) \rightarrow \text{H}(^2\text{S}) + \text{NH}(\text{X}^3\Sigma^-)$ dissociation process. Here, we adopt a procedure used by Lü *et al.*,⁴¹ which successfully fulfilled the transformation between $\text{P}^+(^1\text{D})$ and $\text{P}^+(^3\text{P})$ while constructing the global PES of $\text{PH}_2^+(1^1\text{A}')$.

Thus, the one-body term should be expressed as the $V_{\text{N}(^2\text{D})}$ $f(R)$ switch function, where $V_{\text{N}(^2\text{D})}$ is the potential energy of the $\text{N}(^2\text{D})$ state with respect to that of the $\text{N}(^4\text{S})$ state. With potential energies extrapolated to the CBS limit, the $V_{\text{N}(^2\text{D})}$ equals to $0.08765 E_h$, which agrees well with the experimental value⁴² of $0.08759 E_h$. The $f(R)$ is assumed as the following form^{26,41,43}

$$f(R) = h(R_1)g(r_1) \quad (11)$$

$$h(R_1) = \frac{1}{4} \sum_{i=1}^2 \left\{ 1 - \tanh \left[\alpha_i (R_1 - R_1^{i0}) + \beta_i (R_1 - R_1^{i1})^3 \right] \right\} \quad (12)$$

$$g(r_1) = 0.5 \{ 1 + \tanh[\alpha_0(r_1 - r_1^0)] \} \quad (13)$$

where R_1 is the H-H bond length, r_1 is the length from the N atom to the center of the mass for H-H. In the $\text{N}(^2\text{D}) + \text{H}_2(\text{X}^1\Sigma_g^+)$ channel, the function $h(R_1)$ ensures the decay from the $\text{N}(^2\text{D})$ state to the $\text{N}(^4\text{S})$ state as the H-H bond length increases. The amplitude function $g(r_1)$ is employed to guarantee that eqn (12) only works at the long N-H₂ bond lengths (larger than $8 a_0$). All parameters are obtained by fitting the *ab initio* points and are shown in the ESI.†

3.2 Two-body terms

In the CHIPR method,³⁰ the two-body terms included the coulombic interaction are given by

$$V_i^{(2)}(R_i) = \frac{Z_A Z_B}{R_i} \sum_{k=1}^L C_k y^k \quad (14)$$

where $i = 1, 2, 3$ (1 for H₂, 2 and 3 for NH, respectively), Z_A and Z_B represent the nuclear charges of the A and B atoms, respectively. C_k values are the coefficients of a L th-order polynomial, which are obtained from the least-squares fitting. The numerical coefficients of H₂(X¹Σ_g⁺) and NH(X³Σ[−]) are displayed in the ESI.[†]

3.3 Three-body terms

In the CHIPR method, the three-body term of eqn (5) assumes the form

$$V^{(3)} = \sum_{i,j,k=0}^L C_{i,j,k} \left\{ \sum_{g \in G} p_g^{(i,j,k)} [y_1^i y_2^j y_3^k] \right\} \quad (15)$$

where $C_{i,j,k}$ are expansion coefficients, y_i ($i = 1, 2, 3$; 1 for H₂, 2 and 3 for NH, respectively) has the form of eqn (6), and $p_g^{(i,j,k)}$ is the operator that reflects the permutation symmetry of atoms in a subgroup G of the S_3 symmetric group.⁴⁶ For more details, see Rocha's works.^{47,48} Moreover, i, j and k should satisfy the constraints of $i + j + k \neq i \neq j \neq k$ and $i + j + k \leq L$ to exclude any two-body energies.

4 Features of the PES

The experimentally-refined potential energy curves (PECs) are obtained in a two-step approach. First, the diatomic curves for H₂(X¹Σ_g⁺) and NH(X³Σ[−]) are respectively obtained by fitting 71 and 264 *ab initio* MRCI(Q)/CBS energy points using eqn (14). Then the obtained PECs are refined with the experimental spectroscopic data^{44,45} in the CHIPR 4.0 program.⁴⁸ Fig. 1 shows the fitting CHIPR PECs and deviations between *ab initio* energies and fitted energies of H₂(X¹Σ_g⁺) and NH(X³Σ[−]). The vibrational levels of the experimentally-refined PECs are obtained by the LEVEL program⁴⁹ and presented in Table 1. Good agreement is found when compared with the experimental vibrational levels.^{44,45} The spectroscopic constants of the CHIPR and experimentally-refined CHIPR two-body terms for H₂(X¹Σ_g⁺) and NH(X³Σ[−]) are also determined using Dunham expansion and presented in Table 2, along with the previous theoretical and experimental results.^{50–54} The experimentally-refined PECs significantly improved the spectroscopic constants. The experimentally-refined PECs reproduce accurately the experimental vibrational levels with rmsds of 0.02 and 0.11 cm^{−1} for H₂ and NH, respectively.

The partial and accumulated rmsds of the global NH₂(X²A'') CHIPR PES are listed in Table 3. As shown in Table 3, all 7970 *ab initio* points include an energy range above the global minimum (GM) of NH₂(X²A'') and up to 1000 kcal mol^{−1}. The rmsd around the equilibrium structure (energy within

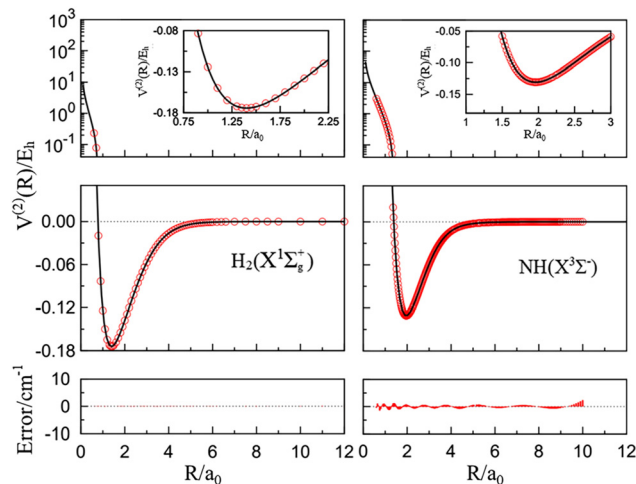


Fig. 1 Potential energy curves of H₂(X¹Σ_g⁺) and NH(X³Σ[−]). Circles represent the *ab initio* MRCI(Q)/CBS energy points, the lines indicate the diatomic curves using eqn (14), and the fitting error is defined by the difference between fitted and original potential energies.

Table 1 The vibrational levels (in cm^{−1}) of H₂(X¹Σ_g⁺) and NH(X³Σ[−]) refined with the experimental spectroscopic data

ν	H ₂ (X ¹ Σ _g ⁺)		NH(X ³ Σ [−])	
	Exp. ⁴⁴	This work	Exp. ⁴⁵	This work
0	0.00	0.00	0.00	0.00
1	4161.14	4161.14	3125.57	3125.56
2	8086.93	8086.94	6094.87	6094.85
3	11782.36	11782.34	8907.59	8907.60
4	15250.31	15250.33	11562.32	11562.43
5	18491.92	18491.91	14056.15	14056.35
6	21505.78	21505.78	16384.35	16384.21

Table 2 The spectroscopic constants of H₂(X¹Σ_g⁺) and NH(X³Σ[−])

	R_e/a_0	D_e/eV	ω_e/cm^{-1}	$\omega_e x_e/\text{cm}^{-1}$
H ₂ (X ¹ Σ _g ⁺)				
This work ^a	1.401	4.742	4420.55	123.54
This work ^b	1.401	4.747	4404.00	119.71
Exp. ⁵⁰	1.401	4.748	4401.21	121.33
Theor. ⁵¹	1.401	4.711	4389.66	121.56
Theor. ⁵²	1.401	4.754	4406.41	121.61
NH(X ³ Σ [−])				
This work ^a	1.962	3.56	3287.37	79.11
This work ^b	1.958	3.55	3281.40	76.83
Exp. ⁵³	1.958	3.55	3282.27	78.35
Theor. ⁵⁴	1.965	3.34	3198.60	82.71

^a Fitted by *ab initio* energies using the CHIPR functional form of eqn (14). ^b Obtained from the experimentally-refined CHIPR potentials, see the text for details⁴⁸

40 kcal mol^{−1}) is 24.47 cm^{−1}, and the max error is 201.23 cm^{−1}. Meanwhile, the total rmsd of the fitting PES is 55.7 cm^{−1}, showing high precision of the present PES.

Based on the accurate CHIPR PES, its stationary points are obtained and compared with the previous works,^{7,24,26,55,56} as

Table 3 The stratified rmsd (in cm^{-1}) of the $\text{NH}_2(\text{X}^2\text{A}')$ CHIPR PES

Energy ^a	N ^b	Max error ^c	Rmsd	N > rmsd ^d
10	263	49.58	16.23	88
20	520	51.77	18.29	167
30	813	201.23	21.31	218
40	1009	201.23	24.47	245
50	1197	201.23	27.71	282
60	2181	201.23	29.98	335
70	2679	202.56	32.55	383
80	3243	206.22	34.02	436
90	3728	206.22	35.47	505
100	4479	212.20	38.15	600
200	7866	354.95	54.91	1633
300	7898	354.95	55.21	1632
500	7936	354.95	55.43	1642
1000	7970	354.95	55.71	1647

^a Energy in kcal mol^{-1} . ^b Number of the calculated *ab initio* energy points up to the indicated energy range. ^c The max error (in cm^{-1}) up to the indicated energy range. ^d Number of the calculated *ab initio* energy points with the energy deviation larger than the rmsd.

shown in Table 4, where R_1 , R_2 and R_3 are the bond lengths of NH_1 , NH_2 and H_1H_2 , respectively. The predicted structure of the GM point is $R_1 = R_2 = 1.938 a_0$ and $R_3 = 3.023 a_0$, which fits well with the theoretical and experimental results.^{7,24,26,55,56} The three harmonic vibrational frequencies differ from the corresponding experimental values by 0.36%, 0.57% and 1.5%, respectively. The predicted energy of the C_{2v} barrier is $0.31 \text{ kcal mol}^{-1}$ higher than that obtained by the DMBE PES of Li *et al.*,⁷ and $0.1 \text{ kcal mol}^{-1}$ higher than that deduced from the RKHS PES of Ho *et al.*²⁴ The barrier heights and bond lengths of other stationary points are all in good agreement with other previous results.^{7,24,26} Meanwhile, the attributes of the van der Waals stationary points, including the equilibrium bond lengths, vibrational frequencies and energies related to the $\text{N}(\text{D}) + \text{H}_2(\text{X}^1\Sigma_g^-)$ or $\text{N} + \text{H}(\text{S}) + \text{H}(\text{S})$ asymptote, also show minor differences with the previous results,⁷ which guarantee the accuracy at the low collision energies.

The topographical contour plots of the $\text{NH}_2(\text{X}^2\text{A}')$ CHIPR PES are illustrated in Fig. 2 and 3. As shown, all plots are smooth and reasonable over the entire configuration space. The panel (a) of Fig. 2 shows the contour plot of the equilibrium configuration with the bending angle fixed at 102.5° . Here, the GM point is the unique and notable feature located at $R_{\text{NH}} = 1.2938 a_0$ and $R_{\text{HH}} = 3.032 a_0$, which agrees well with the observed and calculated values.^{7,24,26,55,56} Fig. 2(b) shows the contour plot as the $\text{N}(\text{D})$ atom inserts into H_2 along the C_{2v} symmetry, which illustrates the C_{2v} barrier at $R_{\text{NH}} = 4.15 a_0$, $R_{\text{HH}} = 1.42 a_0$, and the $D_{\infty h}$ stationary point (SP) at $R_{\text{NH}} = 1.87 a_0$ and $R_{\text{HH}} = 3.74 a_0$, respectively. Fig. 2(c) displays the major features of the linear $[\text{H}-\text{N}-\text{H}]$ geometry. The notable feature is the $D_{\infty h}$ SP with a well depth of $-94.08 \text{ kcal mol}^{-1}$ relative to the $\text{N}(\text{D}) + \text{H}_2$ asymptote and $-0.2368 E_h$ relative to the $\text{N}(\text{D}) + \text{H}(\text{S}) + \text{H}(\text{S})$ asymptote. The prediction agrees well with that of Li *et al.*,⁷ who found that the energy of SP was $95.19 \text{ kcal mol}^{-1}$ below the $\text{N}(\text{D}) + \text{H}_2$ asymptote and $0.2393 E_h$ below the $\text{N}(\text{D}) + \text{H}(\text{S}) + \text{H}(\text{S})$ asymptote. Owing to the exchange of two H atoms, Fig. 2(a)

Table 4 The stationary points on the CHIPR PES of $\text{NH}_2(\text{X}^2\text{A}')$ along with the available experimental and theoretical values

Feature	R_1/a_0	R_2/a_0	R_3/a_0	E^b	E^c	ω_1/cm^{-1}	ω_2/cm^{-1}	ω_3/cm^{-1}
Global min (GM)								
This work ^a	1.938	1.938	3.023	-0.2903	-127.66	3362	3461	1547
Theor. ⁷	1.937	1.937	3.029	-0.2923	-128.45	3370	3557	1570
Theor. ²⁶	1.941	1.941	3.029	-0.2858	-126.4	3383	3457	1541
Theor. ²⁴	1.940	1.940	3.040		-126.4	3350	3436	1559
Exp. ^{55,56}	1.938	1.938	3.040			3374	3481	1524
C_{2v} transition state (TS)								
This work ^a	4.15	4.15	1.42	-0.0830	1.90	4274	440	411
Theor. ⁷	3.98	3.98	1.42	-0.0851	1.59	4256	616	440
Theor. ²⁶	3.93	3.93	1.42	-0.0809	2.16	4209	499	282
Theor. ²⁴	4.05	4.05	1.42		1.8	4240	499	325
$C_{\infty v}$ stationary point								
This work ^a	4.36	2.88	1.48	-0.0798	4.43	2904	1076	804
Theor. ⁷	4.41	2.88	1.53	-0.0794	5.15	2954	1336	1197
Theor. ²⁶	4.41	2.90	1.51	-0.0763	5.1	2671	1455	844
Theor. ²⁴	4.47	2.93	1.54		4.8	2621	1032	764
$D_{\infty h}$ stationary point								
This work ^a	1.87	1.87	3.74	-0.2368	-94.08	3618	7269	1784
Theor. ⁷	1.88	1.88	3.76	-0.2393	-95.19	4075	7010	1596
Theor. ²⁴	1.87	1.87	3.74	-0.2320	-92.66	3676	6979	1544
van der Waals stationary points								
C_{2v} min ^d								
This work ^a	5.94	5.94	1.41	-0.0884	-0.962	4526	232	140
Theor. ⁷	5.95	5.95	1.41	-0.0884	-0.522	4350	170	102
$C_{\infty v}$ TS ^e								
This work	4.91	6.87	1.96	-0.1322	-0.06 ^f	3275	239	50
Theor. ⁷	4.92	6.88	1.97	-0.1320	-0.26 ^f	3255	207	38

^a Fitted by the *ab initio* energies using the CHIPR method. ^b Energies (in E_h) relative to the $\text{N}(\text{D}) + \text{H}(\text{S}) + \text{H}(\text{S})$ asymptote. ^c Energies (in kcal mol^{-1}) relative to the $\text{N}(\text{D}) + \text{H}_2$ asymptote. ^d van der Waals minimum. ^e van der Waals transition state. ^f Energies (in kcal mol^{-1}) relative to the $\text{NH}(\text{X}^3\Sigma^-) + \text{H}$ asymptote.

and (c) show perfect symmetry of the central axis of two H atoms. Fig. 2(d) illustrates the $C_{\infty v}$ SP of the collinear $[\text{N}-\text{H}-\text{H}]$ geometry. Due to the leakage in the deep potential well, this geometry is an unstable structure and its barrier shows good comparison with the previous values.^{7,24,26}

Fig. 3(a) shows the energy contour for a N atom moving around the H_2 molecule with the bond length fixed at $R_{\text{HH}} = 1.401 a_0$. Fig. 3(b) shows the plot for a H atom moving around the NH molecule with the bond distance fixed at $R_{\text{NH}} = 1.938 a_0$. As shown in Fig. 3(a), there is a C_{2v} minimum corresponding to the van der Waals stationary point as shown in Table 4. These two plots are smooth both at the short and long-range regions, which ensures the accuracy of the fitting results for the CHIPR PES.

To better present all major topographical features of the CHIPR PES, the relaxed triangular plot⁵⁷ is illustrated in Fig. 4,

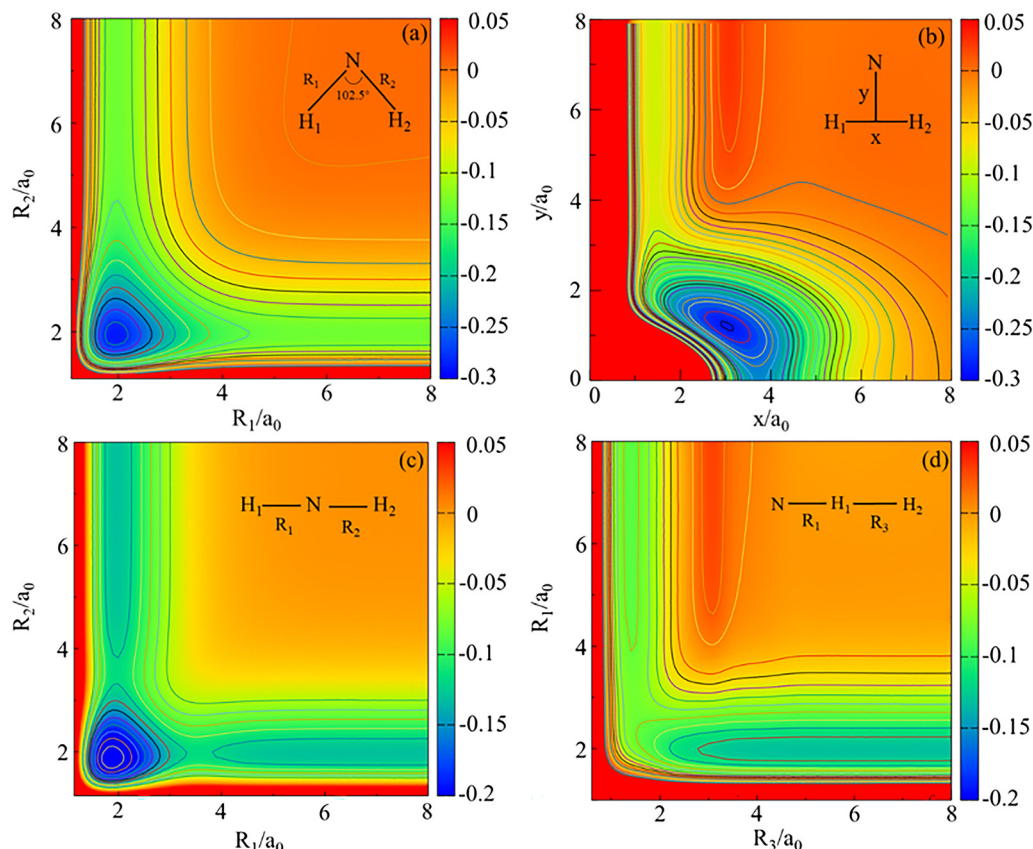


Fig. 2 The contour plots (a) at the fixed included angle $\angle[\text{H-N-H}] = 102.5^\circ$, (b) for the C_{2v} insertion of N into H_2 , (c) for the linear $[\text{H-N-H}]$ geometry, (d) for the linear $[\text{N-H-H}]$ geometry. Contours are equally spaced by $0.02 E_h$ for (a) and $0.13 E_h$ for the others, starting at $-0.3 E_h$ for (a) and (b), $-0.2 E_h$ for (c) and (d).

which utilizes the scaled hyper-spherical coordinates ($\beta^* = \beta/Q$ and $\gamma^* = \gamma/Q$)

$$\begin{pmatrix} Q \\ \beta \\ \gamma \end{pmatrix} = \begin{pmatrix} 1 & 1 & 1 \\ 0 & \sqrt{3} & -\sqrt{3} \\ 2 & -1 & -1 \end{pmatrix} \begin{pmatrix} R_1^2 \\ R_2^2 \\ R_3^2 \end{pmatrix} \quad (16)$$

All stationary points discussed above are shown in Fig. 4. Based on this plot, the connectivity of each stationary point can be established in a more multidimensional way.

5 Dynamic study on the $\text{N}(^2\text{D}) + \text{H}_2(\text{X}^1\Sigma_g^+)$ reaction

Based on the CHIPR PES, the total ICSS and rate constants are used for the $\text{N}(^2\text{D}) + \text{H}_2(\text{X}^1\Sigma_g^+)$ reaction by utilizing the QCT and TDWP methods. The QCT method used here is widely described in the literature.⁵⁸ The TDWP method used in our calculation was first proposed by Zenghui Zhang^{59–61} of New York University in 1993 and developed by the Han's research group.^{61–67}

In the QCT method, 100 000 trajectories are chosen for each collision for calculation to ensure accuracy. To guarantee the

conservation of the total energy within $0.01 \text{ kcal mol}^{-1}$ or smaller, the time integration step of the classical motion equation is chosen to be 0.2 fs in each trajectory. In addition, the initial distance between the N atom and the H_2 molecule is set as 15 \AA to eliminate the influence of the initial interaction energy between two reactants. The ICSSs of $\text{N} + \text{H}_2(v, j) \rightarrow \text{H} + \text{NH}$ are calculated by

$$\sigma_r(v, j) = \pi b_{\text{max}}^2 \frac{N_r}{N} \quad (17)$$

where N_r is the number of the reactive trajectories and N represents the total number of the trajectories, and b_{max} is the maximum impact parameter. The rate constant is given by:⁷¹

$$k(T) = g_c(T) \left(\frac{8k_B T}{\pi \mu_{\text{N+HH}}} \right)^{1/2} \pi b_{\text{max}}^2 \frac{N_r}{N} \quad (18)$$

where $\mu_{\text{N+HH}}$ is the reduced mass of the reactants, k_B is the Boltzmann constant. And the 68% associated error bars are given by $\Delta k = k \left(\frac{N - N_r}{N N_r} \right)^{1/2}$. As the dynamic calculations are performed adiabatically on the $\text{X}^2\text{A}''$ state PES, the electronic degeneracy factor assumes the expression:⁷²

$$g_c(T) = q_{\text{NH}_2}(T) q_{\text{N}^2\text{D}}^{-1}(T) q_{\text{H}_2}^{-1}(T) \quad (19)$$

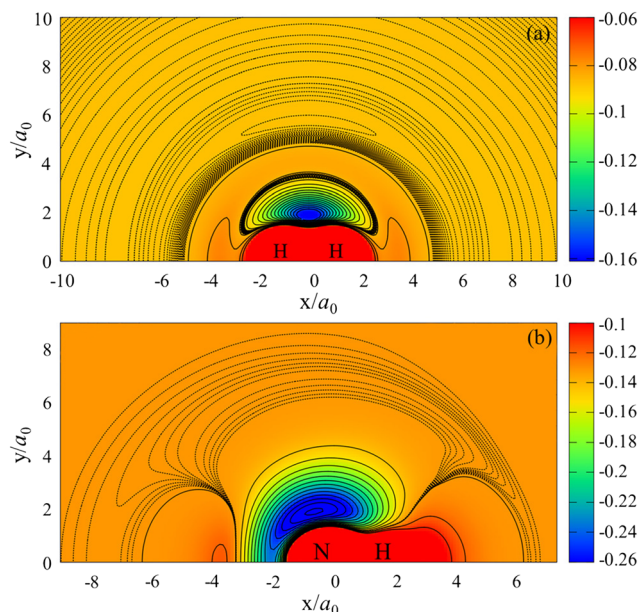


Fig. 3 The contour plot for (a) the N atom moving around the H₂ diatomic molecule which lies along the X-axis with the center being fixed at the origin ($R_{HH} = 1.401 a_0$). The contours are equally spaced by $0.005 E_h$, starting at $-0.17 E_h$. The dashed areas are the contours equally spaced by $0.00001 E_h$, starting at $-0.0883 E_h$. (b) The H atom moves around the NH diatomic molecule, which lies along the X-axis with the center being fixed at the origin ($R_{NH} = 1.938 a_0$). The contours are equally spaced by $0.012 E_h$, starting at $-0.3 E_h$. The dashed areas are the contours equally spaced by $0.00012 E_h$, starting at $-0.1329 E_h$.

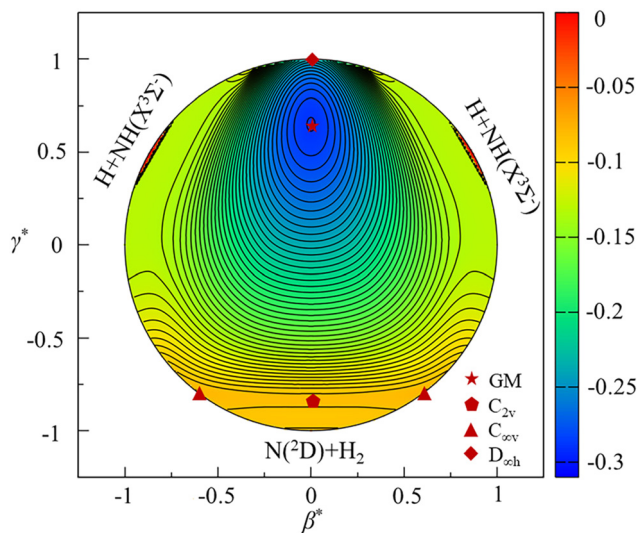


Fig. 4 The relaxed triangular plot of the $NH_2(X^2A'')$ CHIPR PES in hyper-spherical coordinates. The positions and interconnections of all stationary points are illustrated. The contours start at $0.31 E_h$ and are equally spaced by $0.005 E_h$. The positions of all stationary points are indicated explicitly.

where $q_{NH_2} = 2$ is the degeneracy of the ground state NH_2 and the electronic partitions accounting for the fine structure of $H_2(X^1\Sigma_g^+)$ and $N(^2D)$:

$$q_{H_2}(T) = 1 \quad (20)$$

$$q_{N(^2D)}(T) = 6 + 4 \exp(-12.53/T) \quad (21)$$

In the TDWP method,⁷³ the Schrodinger equation was solved using the split-operator scheme. For a triatomic reaction, the Hamiltonian in the reactants's Jacobi coordinates can be written as

$$H = -\frac{\hbar^2}{2\mu_R} \frac{\partial^2}{\partial R^2} + \frac{(\hat{J} - \hat{j})^2}{2\mu_R R^2} + \frac{\hat{j}^2}{2\mu_r r^2} + V(R, r) + h(r) \quad (22)$$

where R indicates the distance between the N atom and the center-of-mass of H₂, r indicates the diatomic distance of H₂, μ_R is the reduced mass between N and H₂, μ_r is the reduced mass of H₂, \hat{J} is the total angular momentum and \hat{j} is the rotational angular momentum of H₂, $V(R, r)$ is the CHIPR PES for $NH_2(X^2A'')$, and $h(r)$ is the diatomic reference Hamiltonian assuming the expression

$$h(r) = -\frac{\hbar^2}{2\mu_r} \frac{\partial^2}{\partial r^2} + V(r) \quad (23)$$

where $V(r)$ is the diatomic potential function.

The wave packet is expanded in terms of a body-fixed translational-vibrational-rotational basis set as

$$\Psi_{v_0 j_0 k_0}^{JK\varepsilon}(R, r, t) = \sum_{n v j k} F_{n v j k, v_0 j_0 k_0}^{JK\varepsilon}(t) u_n^v(R) \phi_v(r) Y_{j k}^{JK\varepsilon}(R, r) \quad (24)$$

where $u_n^v(R)$ is the translational basis, $\phi_v(r)$ is the vibrational basis, and $Y_{j k}^{JK\varepsilon}$ is the rotational basis. The (v_0, j_0, k_0) is the initial rovibrational state of H₂, n is the translational basis label, K and k are the projection quantum number of $J(j)$ on the space-fixed z axis, and ε is the system parity.

The dynamic information is extracted from the final wave packet after a long propagation time, and the total reaction ICS and temperature-dependent rate constant can be calculated by

$$\sigma_{v_0 j_0 k_0}(E) = \frac{\pi}{k^2} \sum_J (2J+1) P_{v_0 j_0 k_0}^J(E) \quad (25)$$

$$\sigma_{v_0 j_0}(E) = \frac{1}{2j_0 + 1} \sum_{k_0} \sigma_{v_0 j_0 k_0}(E)$$

$$k_{v_0 j_0}(T) = \sqrt{\frac{8k_B T}{\pi \mu_R}} (k_B T)^{-2} \int_0^\infty E \sigma_{v_0 j_0}(E) \exp\left(-\frac{E}{k_B T}\right) dE \quad (26)$$

where $P_{v_0 j_0 k_0}^J(E)$ is the reaction probability, k is the wavenumber corresponding to the initial state at a fixed collision energy E , and k_B is the Boltzmann constant. The parameters used in the time-dependent wave packet calculations have been provided in the ESI.†

The total ICSs of the $N + H_2 (v = 0, j = 0) \rightarrow H + NH$ reaction in the present work and previous studies^{4,68–70} are shown in Fig. 5 over the collision energy range of 0–0.8 eV. As can be seen, our ICSs show good comparison with the previous values.^{4,68–70} Since there is a tiny barrier on the minimum energy path, the ICSs elevate drastically with the increasing collision energy and then reach a plateau at the high collision energies. Besides, the relatively higher height of the barrier

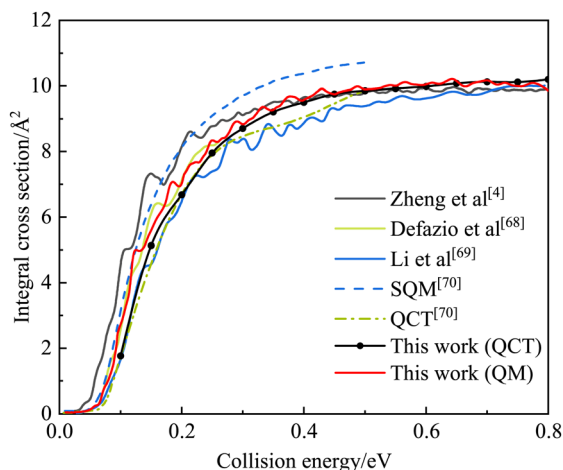


Fig. 5 The integral cross sections (\AA^2) for the $\text{N} + \text{H}_2$ ($v = 0, j = 0$) \rightarrow $\text{H} + \text{NH}$ reaction as a function of the collision energy, along with the previous results.^{4,68–70}

($1.90 \text{ kcal mol}^{-1}$) for the present CHIPR PES may result in the slightly smaller amplitude of the current ICSs.

The total ICSs of each vibrational and rotational state for the $\text{N} + \text{H}_2$ ($v = 0, 1; j = 0, 4, 6, 8, 10$) \rightarrow $\text{H} + \text{NH}$ reaction as a function of the collision energy are given in Fig. 6. As shown, both vibrational and rotational excitations of the reactant H_2 have positive effects on the ICSs. The amplitudes of the vibrational excitations for the ICSs are larger than those of the rotational excitations at the same level of the collision energy, which also has been found in the previous studies.^{23,24,74} This phenomenon indicates that the vibrational and rotational excitations of the reactant promote the effective transfer of the collision energies into the internal energies.⁷⁵ The trends of all ICSs are consistent, which increase drastically and then reach a plateau. For the given vibrational quantum number $v = 0$, the ICSs for the rotational quantum numbers $j = 0, 4, 6$ tend to be identical for the 0.1 to 0.15 eV collision energy range, which indicates that the effect of the rotational excitation on the ICSs is not obvious at the low collision energies when the rotational quantum number equals 0. When $v = 1$, all ICSs grow with the growth of the rotational quantum numbers j at the same collision energy.

The total ICSs of each vibrational state for the $\text{N} + \text{H}_2$ ($v = 0, 1, 2, 3, 4; j = 0$) \rightarrow $\text{H} + \text{NH}$ reaction as a function of the collision energy are shown in Fig. 7. As shown, when the value of v is less than 3, the corresponding ICSs show the same trend, which increase rapidly with the collision energy and level off at the high collision energy. However, when $v = 4$, the ICSs increase at first and then decrease with the growth of the collision energies. In general, the increased vibrational quantum numbers promote the interval energy of the reactant. But the exorbitant initial energy of the reactant may be higher than the barrier in the reaction, which restrains the reaction and reduces the ICSs.

Table 5 lists the experimental room-temperature rate constants^{14–22,76} and our QCT and QM results. The rate obtained using the QCT method appears to underestimate the

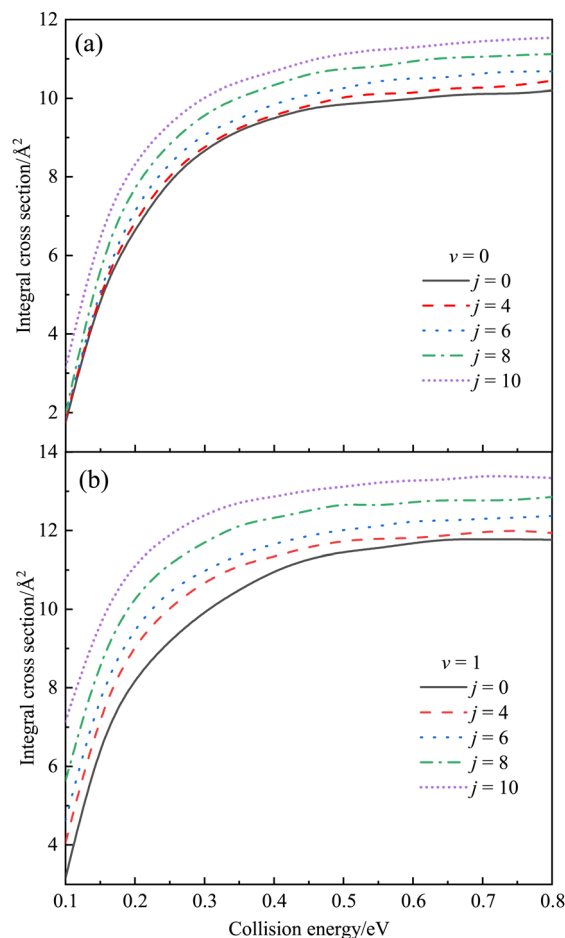


Fig. 6 The integral cross sections (\AA^2) for the $\text{N} + \text{H}_2 \rightarrow \text{H} + \text{NH}$ reaction as a function of the collision energy for several rotational quantum numbers $j = 0, 4, 6, 8, 10$ with the vibrational quantum under (a) $v = 0$, (b) $v = 1$.

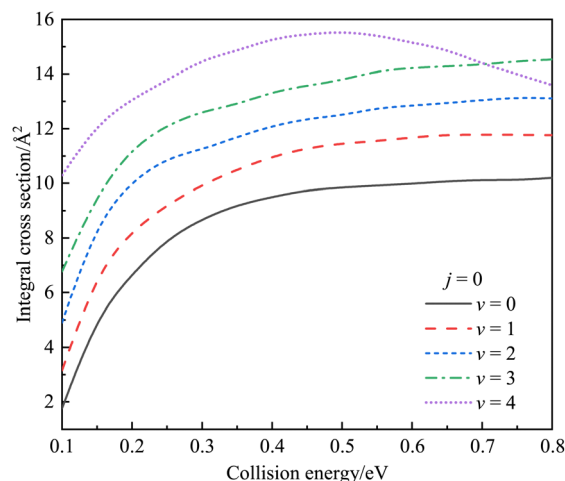


Fig. 7 The integral cross sections (\AA^2) for the $\text{N} + \text{H}_2 \rightarrow \text{H} + \text{NH}$ reaction as a function of the collision energy for several vibrational quantum numbers $v = 0, 1, 2, 3, 4$ with the vibrational quantum number under $j = 0$.

Table 5 The rate constants at the room temperature ($T = 300$ K) for the $\text{N}(\text{D}) + \text{H}_2$ reaction along with the available experimental data and our calculated values

Source	$k/10^{-13} \text{ cm}^3 \text{ s}^{-1}$
Umemoto <i>et al.</i> ¹⁶	22.8 ± 2.3
Fell <i>et al.</i> ¹⁷	35.0 ± 10.0
Husain <i>et al.</i> ¹⁸	21.0 ± 3.0
Husain <i>et al.</i> ¹⁹	17.0 ± 5.0
Black <i>et al.</i> ²⁰	427.0 ± 2.0
Black <i>et al.</i> ⁷⁶	50.0
Whitefield ²¹	18.0 ± 8.0
Piper <i>et al.</i> ²²	23.0 ± 5.0
Suzuki <i>et al.</i> ¹⁴	24.4 ± 3.4
Dianailys <i>et al.</i> ¹⁵	22.35 ± 4.55
This work (QCT)	16.92 ± 0.62
This work (QM)	28.37

experimental values, while the QM result shows good agreement with the experimental values.^{14–16,18} In addition, the rate constants *versus* temperatures are computed and displayed in Fig. 8, along with the earlier experimental and theoretical results.^{14,15,68,73} Clearly, our QCT rate constants largely coincide with the QCT ones of Varandas *et al.*⁷³ Because the quantum tunneling effect and the zero-point energy leakage problem are not considered, the calculated QCT results are systematically lower than the experimental values by about a factor of 2.2 for the temperatures below 300 K. For the TDWP calculations, the

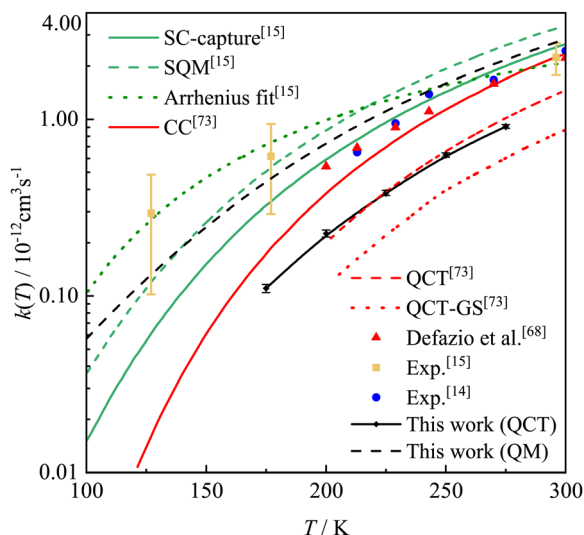


Fig. 8 The rate constants (k) as a function of the temperature (T). The green solid line corresponds to the QCT capture model including a semi-classical correction for tunneling (SC-capture).¹⁵ The green dashed line corresponds to the statistical quantum mechanical (SQM) method.¹⁵ The green dotted line corresponds to the Arrhenius fit to the rate constants of Dianailys *et al.*¹⁵ The red solid line corresponds to the close coupling wave packet calculation (CC).⁷³ The red dashed line corresponds to the QCT.⁷³ The red dotted line corresponds to the QCT-ground state (QCT-GS).⁷³ The solid red triangles correspond to the QM calculations by Defazio *et al.*⁶⁸ The solid yellow squares correspond to the experimental values obtained by Dianailys *et al.*¹⁵ The solid blue circles correspond to the experimental values obtained by Suzuki *et al.*¹⁴ The black solid line with closed circles corresponds to this work by the QCT. The black dashed line corresponds to this work by QM results.

obtained rate constants were well within the uncertainties of the measured values¹⁵ and were also in excellent agreement with both experimental and theoretical results over the 213–300 K temperature range.

6 Conclusion

In this study, we have calculated *ab initio* energy points based on CBS extrapolated MRCI(T/Q) energies and the CHIPR method is employed to fit an analytical model of the global PES for the ground state $\text{NH}_2(\text{X}^2\text{A}')$. The rmsd of the present PES is 55.7 cm^{-1} , which reflects high-precision fit of the *ab initio* energy points. In order to test the accuracy of the present PES, the equilibrium geometry, energies and vibrational frequencies of the stationary points, which are obtained from the CHIPR PES are discussed in detail and are in line with the previous theoretical and experimental results. Based on the novel PES, the rate constants of the $\text{N}(\text{D}) + \text{H}_2(\text{X}^1\Sigma_g^+) \rightarrow \text{H}(\text{D}) + \text{NH}(\text{X}^3\Sigma^-)$ reaction and the ICSs for $\text{N}(\text{D}) + \text{H}_2(\text{X}^1\Sigma_g^+)$ ($v = 0, 1, 2, 3, 4; j = 0, 4, 6, 8, 10$) are obtained and analyzed using the QCT method. The total ICSs for $v = 0, j = 0$ over the collision energy range of 0–0.8 eV are qualitatively consistent with the previous theoretical results. The initial vibrational and rotational excitations of the reactant will enhance the reactivity and the effect of the vibrational excitation is more significant. Our rate constants are also found to be consistent with the previous theoretical and experimental results.

The supplementary data include the validations of PES, the fitted parameters of the switch function, the parameters used in the time-dependent wave packet calculations, the interpretation of the switch function, and the Fortran code for the CHIPR PES, which can also be obtained online at <https://github.com/Dr-Zhi-Qin/Resource>.

Conflicts of interest

There are no conflicts to declare.

Acknowledgements

This work was financed by the National Natural Science Foundation of China (Grant no. 52106098, 11604179), the Natural Science Foundation of Shandong Province (Grant no. ZR2021QE021, ZR2016AQ18), the China Postdoctoral Science Foundation (2021M701977), the Postdoctoral Innovation Project of Shandong Province and the Postdoctoral Applied Research Project of Qingdao City. The scientific calculations in this article have been done on the HPC Cloud Platform of Shandong University.

Notes and references

- 1 T. V.-T. Mai and L. K. Huynh, *Phys. Chem. Chem. Phys.*, 2019, **21**, 17232–17239.

- 2 S. Nourry and L. Krim, *Phys. Chem. Chem. Phys.*, 2016, **18**, 18493–18499.
- 3 F. Holzmeier, M. Lang, I. Fischer, P. Hemberger, G. Garcia, X. Tang and J.-C. Loison, *Phys. Chem. Chem. Phys.*, 2015, **17**, 19507–19514.
- 4 X. Zheng and Z. Zhu, *Mol. Phys.*, 2020, **118**, e1724339.
- 5 J. Deppe, G. Friedrichs, H.-J. Römmling and H. G. Wagner, *Phys. Chem. Chem. Phys.*, 1999, **1**, 427–435.
- 6 J. Li and H. Guo, *Phys. Chem. Chem. Phys.*, 2014, **16**, 6753–6763.
- 7 Y. Li, J. Yuan, M. Chen, F. Ma and M. Sun, *J. Comput. Chem.*, 2013, **34**, 1686–1696.
- 8 E. F. van Dishoeck, D. J. Jansen, P. Schilke and T. Phillips, *Astrophys. J.*, 1993, **416**, L83.
- 9 A. Dalgarno and J. Black, *Rep. Prog. Phys.*, 1976, **39**, 573.
- 10 Z. Yang, S. Wang, J. Yuan and M. Chen, *Phys. Chem. Chem. Phys.*, 2019, **21**, 22203–22214.
- 11 J. A. Dodd, S. J. Lipson, D. J. Flanagan, W. A. Blumberg, J. C. Person and B. D. Green, *J. Chem. Phys.*, 1991, **94**, 4301–4310.
- 12 H. Umemoto and K.-i Matsumoto, *J. Chem. Phys.*, 1996, **104**, 9640–9643.
- 13 H. Umemoto, T. Asai and Y. Kimura, *J. Chem. Phys.*, 1997, **106**, 4985–4991.
- 14 T. Suzuki, Y. Shihira, T. Sato, H. Umemoto and S. Tsunashima, *J. Chem. Soc., Faraday Trans.*, 1993, **89**, 995–999.
- 15 D. Nuñez-Reyes, C. Bray, K. M. Hickson, P. Larrégaray, L. Bonnet and T. González-Lezana, *Phys. Chem. Chem. Phys.*, 2020, **22**, 23609–23617.
- 16 H. Umemoto, N. Hachiya, E. Matsunaga, A. Suda and M. Kawasaki, *Chem. Phys. Lett.*, 1998, **296**, 203–207.
- 17 B. Fell, I. Rivas and D. McFadden, *J. Phys. Chem.*, 1981, **85**, 224–228.
- 18 D. Husain, S. K. Mitra and A. N. Young, *J. Chem. Soc., Faraday Trans. 2*, 1974, **70**, 1721–1731.
- 19 D. Husain, L. Kirsch and J. Wiesenfeld, *Faraday Discuss. Chem. Soc.*, 1972, **53**, 201–210.
- 20 G. Black, R. Sharpless, T. Slanger and D. Lorents, *J. Chem. Phys.*, 1975, **62**, 4266–4273.
- 21 P. D. Whitefield and F. E. Hovis, *Chem. Phys. Lett.*, 1987, **135**, 454–458.
- 22 L. G. Piper, M. E. Donahue and W. T. Rawlins, *J. Phys. Chem.*, 1987, **91**, 3883–3888.
- 23 L. A. Pederson, G. C. Schatz, T.-S. Ho, T. Hollebeek, H. Rabitz, L. B. Harding and G. Lendvay, *J. Chem. Phys.*, 1999, **110**, 9091–9100.
- 24 T.-S. Ho, H. Rabitz, F. J. Aoiz, L. Bañares, S. A. Vázquez and L. B. Harding, *J. Chem. Phys.*, 2003, **119**, 3063–3070.
- 25 Z.-W. Qu, H. Zhu, R. Schinke, L. Adam and W. Hack, *J. Chem. Phys.*, 2005, **122**, 204313.
- 26 A. Varandas and L. Poveda, *Theor. Chem. Acc.*, 2006, **116**, 404–419.
- 27 T.-S. Chu, K.-L. Han and A. J. Varandas, *J. Phys. Chem. A*, 2006, **110**, 1666–1671.
- 28 Y. Li and A. Varandas, *J. Phys. Chem. A*, 2010, **114**, 9644–9654.
- 29 L. Peng, H. Ma, Y. Lü, C. Zhang, S. Gao, S. Liu and Y. Li, *Mol. Phys.*, 2021, **119**, e1928313.
- 30 A. Varandas, *J. Chem. Phys.*, 2013, **138**, 054120.
- 31 A. Varandas, *J. Chem. Phys.*, 2013, **138**, 134117.
- 32 H. J. Werner, P. J. Knowles and G. Knizia, *MOLPRO, version 2015.1, a package of ab initio programs*, University of Cardiff Chemistry Consultants (UC3), Cardiff, Wales, UK, 2015.
- 33 H.-J. Werner, P. J. Knowles, F. R. Manby, J. A. Black, K. Doll, A. Heßelmann, D. Kats, A. Köhn, T. Korona and D. A. Kreplin, *et al.*, *J. Chem. Phys.*, 2020, **152**, 144107.
- 34 P. J. Knowles and H.-J. Werner, *Chem. Phys. Lett.*, 1985, **115**, 259–267.
- 35 H.-J. Werner and P. J. Knowles, *J. Chem. Phys.*, 1988, **89**, 5803–5814.
- 36 T. H. Dunning Jr, *J. Chem. Phys.*, 1989, **90**, 1007–1023.
- 37 D. Feller, K. A. Peterson and J. Grant Hill, *J. Chem. Phys.*, 2011, **135**, 044102.
- 38 A. Karton and J. M. Martin, *Theor. Chem. Acc.*, 2006, **115**, 330–333.
- 39 A. Varandas, *J. Chem. Phys.*, 2000, **113**, 8880–8887.
- 40 J. N. Murrell, *Molecular potential energy functions*, J. Wiley, 1984.
- 41 Y. L. Lü, S. J. Chai, H. Y. Ma, S. B. Gao and Y. Q. Li, *Mol. Phys.*, 2020, **118**, e1688875.
- 42 A. Kramida, Y. Ralchenko and J. Reader *et al.*, *NIST atomic spectra database (ver. 5.3)*, 2015.
- 43 G. Chen, Z. Qin, J. Li and L. Liu, *Phys. Chem. Chem. Phys.*, 2022, **24**, 19371–19381.
- 44 I. Dabrowski, *Can. J. Phys.*, 1984, **62**, 1639–1664.
- 45 R. Ram and P. Bernath, *J. Mol. Spectrosc.*, 2010, **260**, 115–119.
- 46 B. Sagan, *The symmetric group: representations, combinatorial algorithms, and symmetric functions*, Springer Science & Business Media, 2001, vol. 203.
- 47 C. M. Rocha and A. J. Varandas, *Comput. Phys. Commun.*, 2020, **247**, 106913.
- 48 C. M. Rocha and A. J. Varandas, *Comput. Phys. Commun.*, 2021, **258**, 107556.
- 49 R. J. Le Roy, *J. Quant. Spectrosc. Radiat. Transfer*, 2017, **186**, 167–178.
- 50 K.-P. Huber, *Molecular spectra and molecular structure: IV. Constants of diatomic molecules*, Springer Science & Business Media, 2013.
- 51 Y. Li, P. Zhang and K. Han, *J. Chem. Phys.*, 2015, **142**, 124302.
- 52 S. Chai, H. Ma, Y. Lü, J. Liu and Y. Li, *Mol. Phys.*, 2020, **118**, e1655599.
- 53 J. Malicet, J. Brion and H. Guenebaut, *J. Chem. Phys.*, 1970, **67**, 25–30.
- 54 L. Owono Owono, N. Jaidane, M. Kwato Njock and Z. Ben Lakhdar, *J. Chem. Phys.*, 2007, **126**, 244302.
- 55 J. Demaison, L. Margulès and J. E. Boggs, *Phys. Chem. Chem. Phys.*, 2003, **5**, 3359–3363.
- 56 W. Gabriel, G. Chambaud, P. Rosmus, S. Carter and N. C. Handy, *Mol. Phys.*, 1994, **81**, 1445–1461.
- 57 A. Varandas, *Chem. Phys. Lett.*, 1987, **138**, 455–461.
- 58 G. H. Peslherbe, H. Wang and W. L. Hase, *Adv. Chem. Phys.*, 1999, **105**, 171–201.

- 59 D. H. Zhang and J. Z. Zhang, *J. Chem. Phys.*, 1993, **99**, 6624–6633.
- 60 D. H. Zhang and J. Z. Zhang, *J. Chem. Phys.*, 1994, **101**, 3671–3678.
- 61 J. Z. Zhang, J. Dai and W. Zhu, *J. Phys. Chem. A*, 1997, **101**, 2746–2754.
- 62 X. Zhang, G.-H. Yang, K.-L. Han, M. Wang and J. Z. Zhang, *J. Chem. Phys.*, 2003, **118**, 9266–9271.
- 63 T.-S. Chu and K.-L. Han, *J. Phys. Chem. A*, 2005, **109**, 2050–2056.
- 64 T.-X. Xie, Y. Zhang, M.-Y. Zhao and K.-L. Han, *Phys. Chem. Chem. Phys.*, 2003, **5**, 2034–2038.
- 65 Y. Zhang, T.-X. Xie, K.-L. Han and J. Z. Zhang, *J. Chem. Phys.*, 2003, **119**, 12921–12925.
- 66 Y. Zhang, T.-X. Xie and K.-L. Han, *J. Phys. Chem. A*, 2003, **107**, 10893–10896.
- 67 Y. Zhang, T.-X. Xie, K.-L. Han and J. Z. Zhang, *J. Chem. Phys.*, 2004, **120**, 6000–6004.
- 68 P. Defazio and C. Petrongolo, *J. Chem. Phys.*, 2006, **125**, 064308.
- 69 Z. Li, C. Xie, B. Jiang, D. Xie, L. Liu, Z. Sun, D. H. Zhang and H. Guo, *J. Chem. Phys.*, 2011, **134**, 134303.
- 70 L. Bañares, F. J. Aoiz, T. González-Lezana, V. J. Herrero and I. Tanarro, *J. Chem. Phys.*, 2005, **123**, 224301.
- 71 J. Li, P. J. Caridade and A. J. Varandas, *J. Phys. Chem. A*, 2014, **118**, 1277–1286.
- 72 M. Graff and A. Wagner, *J. Chem. Phys.*, 1990, **92**, 2423–2439.
- 73 A. J. Varandas, T.-S. Chu, K.-L. Han and P. J. Caridade, *Chem. Phys. Lett.*, 2006, **421**, 415–420.
- 74 B. Jayachander Rao and S. Mahapatra, *J. Chem. Phys.*, 2007, **127**, 244307.
- 75 Z. Zhu, H. Wang, X. Wang and Y. Shi, *Mol. Phys.*, 2018, **116**, 1108–1117.
- 76 G. Black, T. Slanger, G. St. John and R. Young, *J. Chem. Phys.*, 1969, **51**, 116–121.